ORIGINAL ARTICLE

The effect of pH on the morphological transformation of nanocrystalline hydroxyapatite during wet chemical synthesis

Anum Ayub Awan[1] · Usman Liaqat[1] [iD] · Zakir Hussain[1] [iD]

Abstract

Hydroxyapatite (HAP) is a prominent bioceramic, notably used in the biomedical field. Fundamental properties of the biomaterials are size and shape dependent. High purity, morphology, and size are the main properties to be addressed for clinical application. Therefore, this work reports the effect of pH and annealing temperature on HAP's shape, crystallite, and particle size. Morphologically different hydroxyapatite nanostructures are synthesised by wet chemical precipitation. Furthermore, the pH of the solution varied from 6 to 11, and the calcination temperature was changed from 300 °C to 900 °C. Various morphologies of hydroxyapatite nanopowders, such as spherical, distorted boxes, aggregated rods, flakes, and beaded rods-like clusters, have been achieved. Moreover, small crystallite and particle sizes of HAP were observed in an alkaline medium. The spherical-shaped hydroxyapatite with particle size between 21.54 nm to 78.89 nm was obtained at pH 11. In contrast, beaded rods, nanorods, nanoflakes and distorted boxes-like morphology with an average particle size between 28.28 nm and 202.43 nm were successfully synthesised in neutral to moderately basic pH. Moreover, the crystallite size between 8.4 to 77.7 nm was achieved by changing the pH and annealing temperature. The synthesised products were analysed by XRD, FTIR, Raman spectroscopy and SEM to determine the crystallinity, purity, chemical composition, vibrational modes, morphology, and particle size.
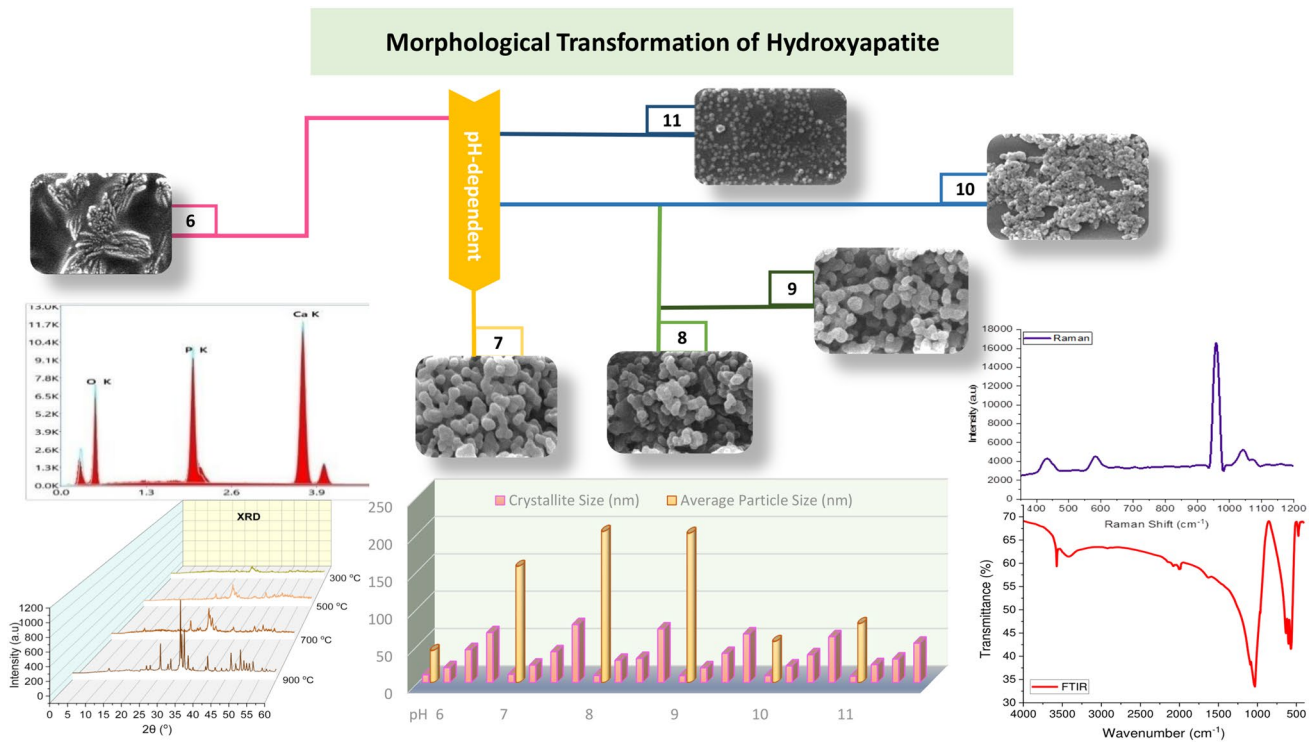
✉ Usman Liaqat
usman.liaqat@scme.nust.edu.pk

Anum Ayub Awan
aayub.phdscme@student.nust.edu.pk

Zakir Hussain
zakir.hussain@scme.nust.edu.pk

[1] School of Chemical and Materials Engineering (SCME),
National University of Sciences and Technology (NUST),
H-12, Islamabad 44000, Pakistan

Graphical abstract

Keywords Bioceramic · Morphological transformation · Hydroxyapatite · pH-dependent synthesis · Bone mineral

1 Introduction

Complex biomaterials like bone, dentin, and enamel have a mineral (e.g., brittle hydroxyapatite) and an organic (e.g., collagen) phase. At the same time, the mechanical strength of the biological apatite at the nanoscale depends on the morphology of the crystalline material [1]. Hydroxyapatite (HAP) is an essential biomaterial with extraordinary properties owing to its specific similarity with hard tissues [2]. Due to the spectacular features of hydroxyapatite [$Ca_{10}(PO_4)_6(OH)_2$], such as porosity, crystallinity, and stoichiometry, it is widely used as a filler for bone defects [3, 4], drug delivery [5–7], bioactive coating materials for various implants [8–11] scaffold for tissue regeneration [12–16]. Hydroxyapatite is a ceramic entity that can be fabricated into different shapes and has high compressive strength [17–20], biocompatibility [21, 22], bioactivity [23], thermodynamic stability in its crystalline state [24, 25], perfect osteoconduction ability [26, 27]. It can be integrated effectively as a bone implant without generating local toxicity and inflammation inside a host body [28]. Such biomaterials have great applicability due to the increased interest in medicine [29].

Natural and synthetic sources are the two existing fabrication routes for hydroxyapatite synthesis [30, 31]. Different approaches have been reported for the synthesis of bone material (hydroxyapatite) such as solid-state synthesis [19, 32], wet-chemical precipitation [33–35], biogenic source [36], the sol–gel method [37], a hydrothermal method [38], pyrolysis [39], combustion [40], hydrolysis [41], sonochemical [42], and through combined microwave and ultra-sonic techniques [43].

The morphological and crystallographic features of hydroxyapatite rely strongly on the reaction parameters (i.e., pH, temperature, pressure, methodology, reaction time, speed of precursor's addition, and the concentration of the reactants) [44–46]. In this regard, different morphologies of hydroxyapatite, such as nanorods, whiskers (40–111 μm), and hexagonal rods (15–38 μm), have been synthesised by changing the temperature, pH, time, and concentration of cations (Ca^+ ions) (Pioterz Szternet et al. in 2022) [47]. Similarly, rod-shaped and bamboo leaf-like morphology of hydroxyapatite have been reported at alkaline pH at 70 °C and 90 °C (I. H. Lee et al. 2020) [48]. A group of researchers illustrated that high alkalinity increased the particle size of hydroxyapatite from 50 to 100 μm (A. Yudin et al. 2019) [49]. Moreover, high alkalinity changed two-phase hydroxyapatite to single-phase crystalline material (K. Chuprunov et al., 2020) [50]. Another group of researchers

demonstrated the effect of pH on the phases of hydroxyapatite (S. Lopez-Ortiz et al.) [51]. They observed a monoclinic phase in a weakly acidic medium. In contrast, they found the formation of hexagonal phase of hydroxyapatite in an alkaline medium.

Moreover, the morphology, orientation, particle and crystallite size significantly impact the material's specific properties for biomedical applications [52–54]. In this context, during cancer treatment, bone tissue regeneration and drug delivery, the morphology and particle size of the nanoparticle are essential to dictate their interaction with the cell membrane [55–58]. Different sizes and morphologies of hydroxyapatite were found to have a significant inhibitory and apoptosis in various tumour cells such as osteosarcoma cancer cells [59], colon cancer cells [60], gastric cancer cells [61], breast [62] and liver cancer cells [63]. In tumour vascularisation, the oblate-shaped nanoparticles are transported via connective means in the tumour microcirculation and have increased lateral drift toward the blood vessels. Recent studies have reported that oblate morphology favours blood circulation due to lower macrophage uptake. Besides this, endocytosis of the normal or cancer cells seems to be dictated by the morphology of the nanoparticle [64]. Moreover, the receptor-ligand interaction is mainly governed by the morphology of the nanoparticles [65]. In addition, ellipsoidal nanoparticles can form multivalent interactions compared to nanospheres. Extensive studies reported that different morphologies such as rod, disc, hemisphere, and ellipsoidal-shaped nanoparticles have enhanced rates of margination and internalisation by the cancer cells compared to spherical-shaped nanoparticles [66].

In bone tissue regeneration, the osteoblast (bone cell) produces osteoid (collagen-rich matrix) normally mineralised by calcium and phosphate ions. Furthermore, the uptake of nanoparticles by the cells at the initial stage affects the cell's proliferation and protein expression. In this regard, a research work demonstrated the initial in-depth study based on the effect of different morphologies of hydroxyapatite (short rods, long rods, needle and spherical) on the inhibition and apoptosis of the osteosarcoma-derived cell lines and found that the spherical-shaped hydroxyapatite nanoparticles decreased the rate of osteoblast cells proliferation compared with long rod-shaped HAP nanoparticles [67]. In addition, this work also reported the self-organisation of the osteoblast cell layers (containing matrix vesicles) and its alteration in the presence of HAP nanoparticle-stimulated groups.

In another study, round-shaped HAP nanoparticles had a more incredible osteogenic effect on bone cells (osteoblast) than spherical HAP [68]. This group also reported that the porous spherical granules of HAP have micro and nano-interconnected channels that can be used for the sustained release of drugs during bone tissue regeneration. However, mesoporous rod-shaped HAP nanoparticles (75–125 nm

in length) have been reported as a suitable drug carrier for protein [69]. They demonstrated the in-vitro studies based on the adsorption and release rate of two proteins, bovine serum albumin (BSA) and lysozyme (LZA), on rod-shaped HAP nanoparticles. They found that the surface charge of the nanoparticles is a vital parameter for the more adsorption and release of the BSA protein over the nanorod-shaped hydroxyapatite. Similarly, ciprofloxacin-loaded alginate-doped hydroxyapatite (needle-shaped) [70] and hydroxyapatite combined with MWCNTs [71] have been reported to prevent infection during bone implant and showed the sustained prolonged profile during drug delivery.

In light of these findings, it can be inferred that the nanoparticles' shape, size and concentration have a significant impact on biomedical applications. So, different parameters related to cell viability and activity are affected by the morphology, concentration and size of the nanoparticles. In addition, various processing parameters, such as pH, temperature and precursor concentration, affect the shape and size of the nanoparticles during synthesis. In this context, a synthetic route is designed to procure the biomaterial with beneficial properties by controlling the shape and size. Here we focus on studying morphology by varying the pH to make it further applicable in the biomedical field with improved bioactivity. This research uses a cost-effective method to analyse the influence of pH and calcination on the shape, crystallite, and particle size of the hydroxyapatite nanostructures.

2 Materials and methods

2.1 Materials

The precursors used in this study were calcium hydroxide (Ca (OH)$_2$, purity 98%) purchased from GPR Rectapur, ortho-phosphoric acid (H$_3$PO$_4$, purity > 85%) purchased from Honeywell (Fluka, USA, NC), ammonium hydroxide solution or ammonia solution, (NH$_4$OH, purity > 95%) from Sigma Aldrich, and ethanol [C$_2$H$_5$OH (EtOH) purity > 97%] was purchased from Sigma Aldrich.

2.2 Characterization methods

The crystallographic characterisation and purity determination of the synthesised products (AYM-1 to AYM-24) were done by using an X-ray diffractometer (XRD-STOE, Germany) using a Ni-Cu (Kα) target at an operating volt of 20 kV, step size of 0.004/min and scan angle of 0°–60°. Furthermore, the presence of different phases was matched with the available motifs in the Joint Committee on Powder Diffraction Standards (JCPDS). Moreover, the Rietveld refinement of all spectrums was done

using the Material Analysis Diffraction (MAUD) Software. The existence of various functional groups was analysed by using the Fourier transform infrared (FTIR) Spectrometer (Perkin Elmer- Spectrum 100, USA) with a frequency range of 400–4000 cm^{-1} having 5 cm resolution, and the samples' holding material was KBr Disc. The intramolecular and vibrational states of the chemical bonds were studied with the Raman microscope and analyser (i-Raman® High-Resolution TE cooled Raman Spectrometer with 1064-nm-Fiber Optic Raman System, USA), which has a resolution in the range of 4.5 cm^{-1} to 614 nm. Nanohydroxyapatite powders' shape, microstructure, and size were examined by scanning electron microscope (SEM, JSM-6490A, JEOL, Japan), equipped with a secondary electron detector (E.T detector) having a resolution of 3 nm. The chemical constitution of the nanopowders was analysed by energy dispersive spectrometry (EDS) coupled with SEM (JSM-6490A). Moreover, the size of the particles was determined by the SEM micrograph processing software via an image.

3 Experimental procedure

3.1 Preparation of hydroxyapatite

Nanohydroxyapatite powders (AYM-1 to AYM-24) were synthesised by the reported protocol [72] with slight modifications, as shown in Fig. 1. In connection with the procedure, the sample codes from AYM-1 to AYM-24 are used to designate the prepared hydroxyapatite samples at different pH and annealing temperatures. Synthesised samples

at pH 6, annealed at 300 °C, 500 °C, 700 °C and 900 °C, were assigned consecutive sample codes such as AYM-1, AYM-2, AYM-3 and AYM-4. Similarly, samples prepared at pH 7, annealed at the temperatures mentioned earlier, were given codes; AYM-5, AYM-6, AYM-7 and AYM-8. For the samples prepared at pH 8 (AYM-9, AYM-10, AYM-11 and AYM-12), pH 9 (AYM-13, AYM-14, AYM-15, AYM-16), pH 10 (AYM-17, AYM-18, AYM-19 and AYM-20) and pH 11 (AYM-21, AYM-22, AYM-23 and AYM-24), they were given sample codes that represent the annealing temperature of 300 °C, 500 °C, 700 °C and 900 °C.

In this procedure, 0.5 molar Ca (OH)$_2$ suspension was reacted with 0.3 molar H$_3$PO$_4$ solution. The molar ratio is consistent with the compositional formula of the mineral Ca$_{10}$(PO$_4$)$_6$(OH)$_2$ [stoichiometric Ca/P ratio = 1.67]. At the same time, the acidity of the reaction mixture was changed from 11 to 6 at different stages throughout the synthetic procedure. The calcium hydroxide suspension (0.5 M) was prepared in deionised water with continuous stirring at 6000 rpm for about one hour at 80 °C. After stirring the rest to the desired temperature, a 0.3 M solution of H$_3$PO$_4$ was added dropwise into the calcium hydroxide suspension, that led to the formation of white precipitates in a reaction mixture. The pH of the reaction mixture was carefully observed with the help of pH paper throughout the reaction, and it was adjusted by adding ammonium hydroxide solution (1 M). After attaining the desired pH, the reaction mixture was stirred for an additional hour at 80 °C. The resulting solution was then aged at room temperature (21 °C) for the next 24 h, excess solution was decanted, and the precipitates were washed
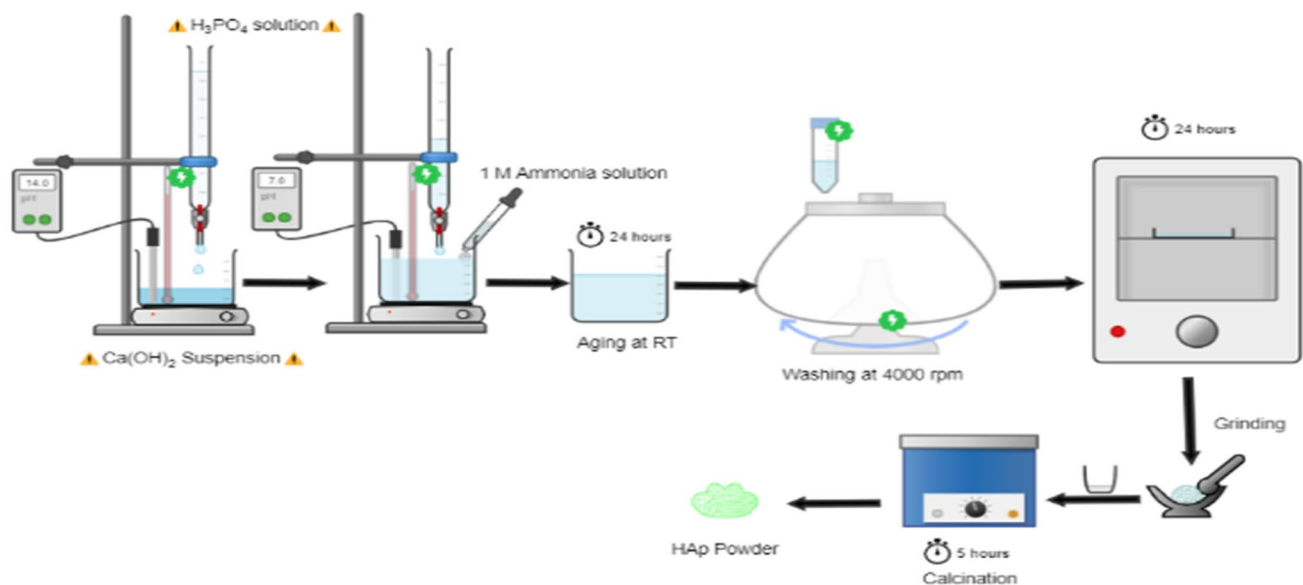
Fig. 1 Illustrative depiction of the synthesis of hydroxyapatite nanopowders (AYM-1 to AYM-24)

three times with 5% EtOH: H_2O mixture by centrifugation (4000 rpm) for 15 to 20 min. The resulting precipitates were dried in an oven for 24 h at 100 °C. After this, the dried products were grounded using mortar-pestle and calcinated with a heating speed of 10 °C/minute in a muffle furnace for 5 h. The obtained products were then further characterised by different techniques. The yield of the products (AYM-1 to AYM-24) synthesised by this protocol is 73–92%, respectively.

Chemical Reaction: $10\,Ca\,(OH)_2 + 6\,H_3PO_4 \rightarrow Ca_{10}(PO_4)_6(OH)_2 + 18\,H_2O$.
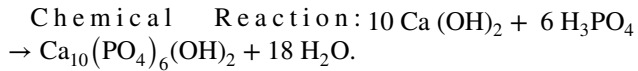
4 Results

4.1 XRD analysis

XRD analysis is performed to elucidate the purity, presence of the phases, and crystallinity of the products (AYM-1 to AYM-24) synthesised during the precipitation method, the X-ray diffractograms of the samples (AYM-1 to AYM-24) are illustrated in Fig. 2(i), which were thermally heated at different annealing temperatures (300 °C, 500 °C, 700 °C and 900 °C). The observed patterns are matched with the JCPDS repository. The major diffraction peaks (2θ) at 10.8°, 25.8°, 31.7°, 32.1° 32.8°, 34.0°, 32.9°, 46.6°, and 49.4° correspond
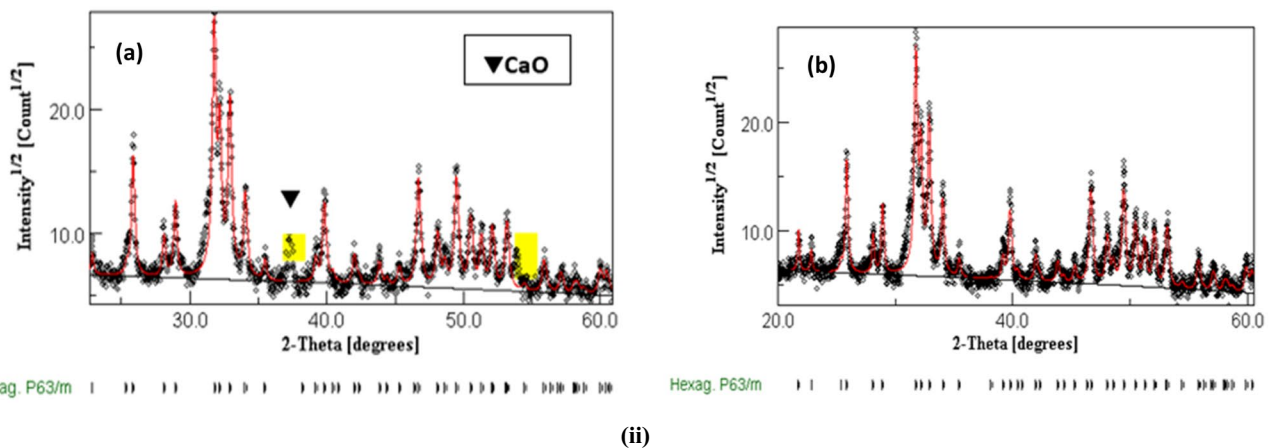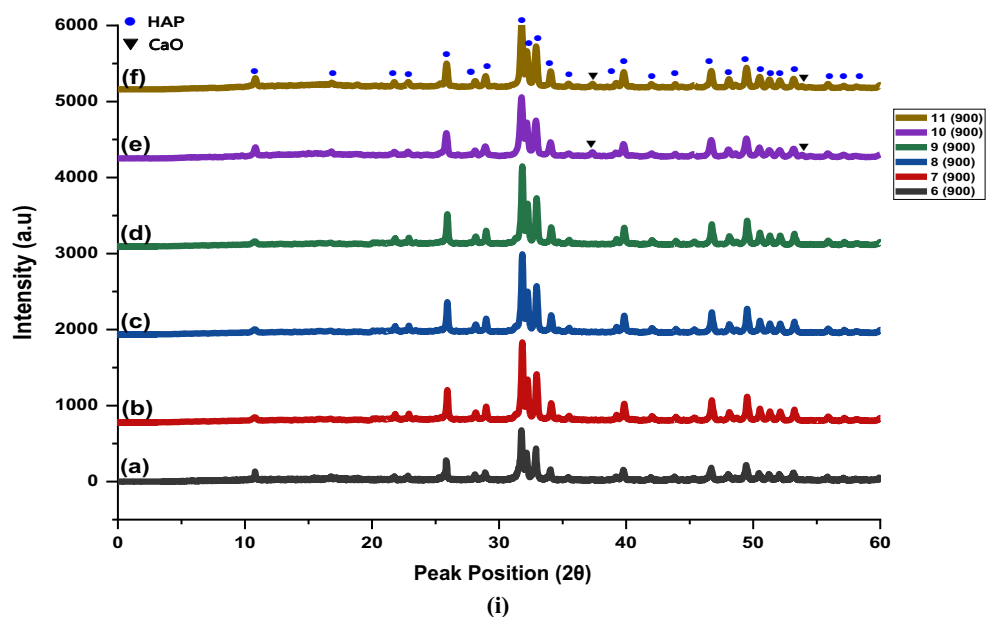
Fig. 2 (**i**) XRD diffractogram of synthesised products at pH (a) 6, (b) 7, (c) 8, (d) 9, (e) 10, and (f) 11 annealed at 900 °C (reference pattern: JCPDS: 74-0566, JCPDS 74-0565). (**ii**) Rietveld refinement plot of the sample prepared at (a) pH 11, showing the presence of CaO phase at 37.6° and 54.2° along with HAP phase (left side) and (b) pH 7—all peaks correspond to the single HAP phase (right side). Black line represents the background and vertical line indicates the Bragg's allowed peaks

to the hexagonal planes (100) (002), (211), (112), (300), (202), (130), (222), and (213) of hydroxyapatite; JCPDS 01-074-0566, JCPDS 01-074-0565 with P6$_3$/m space group. When samples were annealed from low to high temperatures between pH 6 to 9, the XRD diffractograms did not show the development of other distinguishable auxiliary phases, such as ACP, TCP, DCP, and CaO. The least abundant calcium oxide (CaO) phase [73] with the preferential orientation in a plane (200) appeared at 37.6° (2θ) aside from the hexagonal hydroxyapatite phase is observed in the diffractogram of the samples (AYM-20 and AYM-24,), prepared at alkaline pH (10 & 11), and annealed at 900 °C, as illustrated in Fig. 2(i)-(e & f). A single crystalline hydroxyapatite phase is observed below pH 10 calcinated at 300 °C, 500 °C, 700 °C, and 900 °C. The samples annealed at low temperatures (i.e., 300 °C, 500 °C and 700 °C) did not indicate any discriminatory peak of CaO even at a higher alkaline medium (pH = 10 and 11). The XRD diffractogram is used to figure out the crystallite size (D$_{hkl}$) of the products prepared between pH 6 and 11 and calcinated within 300 °C to 900 °C. The determination of crystallite size is valuable for tracking the crystal's size. In addition, this property gives information about the synthesised materials, whether they are brittle with large crystallites or soft having small crystallites. Form the intensities, the full-width half maxima (FWHM) of various synthesised samples (AYM-1 to AYM-24) are measured. The crystallite size of the prepared samples is listed in Table 3 and computed using the Scherrer Eq. (1) [74].

Debye–Scherrer Equation:

$$D = aree \div \beta(\text{hkl}).Cos(\theta), \qquad (1)$$

whereas K is the Scherrer constant, λ is the wavelength of x-ray radiation, $\beta_{(hkl)}$ is the full-width half maxima (FWHM) of the corresponding diffraction plane, and Cos (Θ) is the measured angle of the same plane. XRD diffractograms indicated the amorphous XRD patterns at low annealing temperatures, and crystalline XRD patterns are more pronounced at a high calcination temperature of 900 °C. Figure 7 draws a comparison from the observed patterns, i.e., by increasing the annealing temperature, the diffraction peaks narrow down. At the same time, a decrease in the crystallinity of the nanohydroxyapatite reflects the enlarged full width at half maxima (FWHM) of nearly all diffraction planes shown in Table 2. The development of a new phase of calcium oxide (CaO) at higher pH has been assigned to the existence of an extra amount of calcium stayed during the precipitation, and the sintering of the product to higher temperature converted it to the more stable calcium oxide phase.

4.1.1 Rietveld refinement

This method is used for the evaluation of atomic position, lattice parameters, and occupation parameters. In addition

to this, crystallite size of the products is evaluated by the method provided in Ref [75, 76]. This procedure is convenient to provide information about the material structure. The XRD patterns are analysed, and the observed pattern during refinement is described by the profile parameters, illustrated in Fig. 2(ii). The FWHM, Bragg's reflection, shape, asymmetry model, and the diffraction lines' tails are identical for the complete diffraction pattern. The initial refinement is performed, such as the background parameters, unit-cell, and zero-point shift. A distinct reflection profile fitting is analysed to determine crystallite size. Furthermore, peak asymmetry and related profile parameters are refined for good match peak positions. Figure 2(ii) is a typical Rietveld refinement plot to visualise the peaks obtained between the calculated and measured intensities of the products prepared. The final R-factor (R weight profile) for the hexagonal phase of the prepared samples is 5.87.3–11.24 %. In addition, 1.096–1.557 is the observed goodness-of-fit indicator of the samples. The crystallite size of the samples is calculated from the Rietveld refinement method and obtained between 8.13 and 69.3 nm, listed in Table 3. The obtained values are compared with the Debye–Scherrer method. The difference is fundamental that gives insight into the separation of reflection broadening, resulting in the small strain and crystallite size. In one approach, the internal breath of the Bragg peak is due to strain and size broadening [77]. Figure 2(ii) depicts the structural refinement pattern at pH 7 (b) and at pH 11 (a), based on the hexagonal phase of hydroxyapatite. The residual peak of CaO is observed at 37.6° and 54.2° (marked by yellow colour) at pH 11. All other structural refinements below pH 10 are based on the pure hexagonal phase without indicating secondary phases. The observed crystal system is hexagonal; space group (P 6$_3$/m), lattice parameters (a = b = 9.41898 and c = 6.8819, angle (α = β = 90° and γ = 120°), R (expected)/6.9 % and R (profile)/5.79%, respectively.

4.2 FTIR spectroscopic analysis

The characteristic absorption bands of the synthesised nanopowders (AYM-1 to AYM-24) are shown in Fig. 3; all the band positions concur with the values given in the literature [78, 79]. The results have revealed the asymmetric and symmetric stretching vibrations of each functional group present in the prepared samples (AYM-1 to AYM-24). The relatively wide band position is observed in all samples at 3657 – 3676 cm^{-1} related to the asymmetric vibration (stretching) of hydroxyl (OH) groups. Still, these wide bands become narrower with the temperature rise. The intense IR absorption bands in all spectrums indicate the vibrational modes of necessary building units (PO$_4^{3-}$). The asymmetric stretching bands (v_3 modes in PO$_4^{3-}$) are detected around 1026 – 1049 cm^{-1}, while the symmetric stretching vibration (v_1)
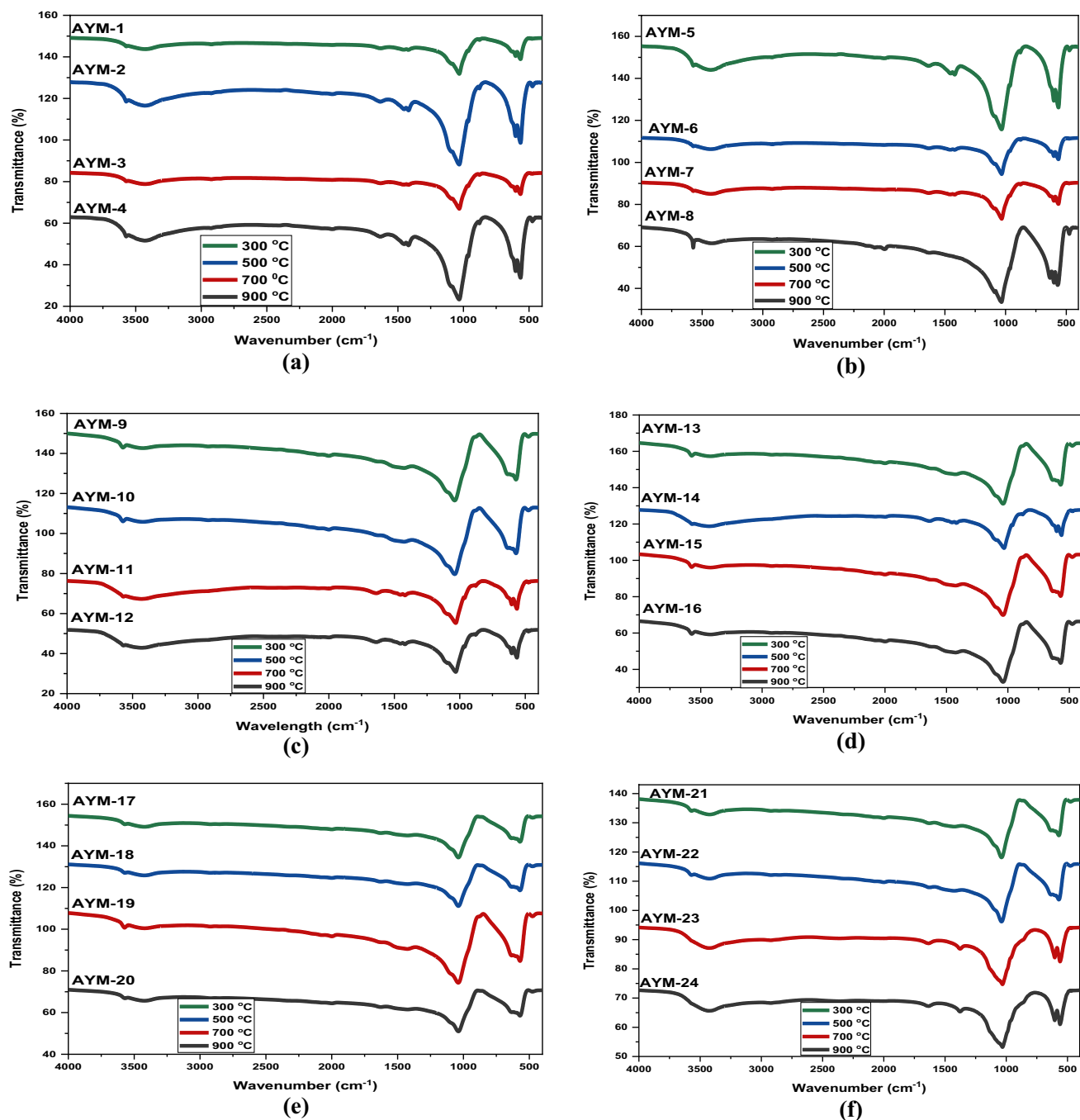
Fig. 3 FTIR spectrographs of morphologically different hydroxyapatite (AYM-1 to AYM-24) prepared at pH **a** 6, **b** 7, **c** 8, **d** 9, **e** 10, and **f** 11 calcinated at different temperatures (300 °C–900 °C)

of PO_4^{3-} is identified in the $956 - 969$ cm^{-1}. The bending vibration of triply degenerate (v_4 and v_2 modes in O–P–O of the apatite (PO_4^{3-}) appeared on the scale of $558 - 579$ cm^{-1} and $601 - 647$ cm^{-1} in the spectrums. The annealed samples exhibit a minor frequency and prominent bands around $2343 - 2356$ cm^{-1} (from 300 °C to 900 °C), mainly attributed to the release of CO_2 during the heat treatment. In addition, the characteristic bands (v_3) correspond to the presence of

carbonate (CO_3^{2-}) ions around $1411-1627$ cm^{-1}. The weak absorption band (v_2) of the CO_3^{2-} ion is inspected in the range of $869 - 885$ cm^{-1}. The FTIR results indicated the successful preparation of nano-hydroxyapatite by the wet chemical precipitation method, clearly showing the presence of two main building block units (PO_4^{3-} and OH). The band positions and the vibrational modes of the essential building blocks of prepared structures are listed in Table 1.

Table 1 The observed IR band values of the different functional groups present in the prepared nano-hydroxyapatite samples (AYM-1 to AYM-24) at different pH (6—11), and calcination temperatures (300 °C–900 °C)

S. No	pH	Samples code	Characteristic bands and wavelength (cm^{-1})					
			PO$_4$$^{3-}$				OH$^-$	CO$_3$$^{2-}$
			v_1 (Symmetric Stretching)	v_2 (Stretching)	v_3 (asymmetric Stretching)	v_4 (Bending)		(C–O)
1	6	AYM-1	966	566	1036	602	3575	1411
		AYM-2	960	569	1037	602	3574	1427
		AYM-3	969	568	1032	601	3575	1416
		AYM-4	962	564	1034	604	3572	1421
2	7	AYM-5	960	565	1033	606	3579	1418
		AYM-6	959	564	1031	600	3577	1413
		AYM-7	962	579	1036	602	3575	1424
		AYM-8	963	572	1030	603	3573	1627
3	8	AYM-9	962	574	1036	643	3580	1450
		AYM-10	966	576	1042	641	3576	1467
		AYM-11	960	563	1026	603	3576	1420
		AYM-12	958	561	1036	601	3572	1419
4	9	AYM-13	957	563	1039	644	3577	1420
		AYM-14	961	560	1023	607	3567	1415
		AYM-15	956	575	1033	646	3574	1434
		AYM-16	960	570	1029	640	3575	1445
5	10	AYM-17	965	572	1030	640	3577	1437
		AYM-18	957	579	1042	645	3572	1452
		AYM-19	969	569	1041	647	3573	1449
		AYM-20	962	570	1046	641	3569	1440
6	11	AYM-21	958	568	1049	644	3564	1459
		AYM-22	957	569	1045	637	3561	1473
		AYM-23	960	558	1031	602	3555	1439
		AYM-24	959	557	1030	604	3547	1412

4.3 Raman spectroscopic analysis

The hydroxyapatite structure has different functional groups, and vibrational spectroscopy is a valuable tool to determine the presence of basic building units (PO$_4$$^{3-}$, OH). The Raman analysis is performed to track the structural composition of the synthesised products (AYM-1 to AYM-24). The observed Raman spectrum of the pure hydroxyapatite synthesised at various pH (i.e., 6–11) and calcination temperatures (300 °C, 500 °C, 700 °C, and 900 °C.) is given in Fig. 4. All wavenumbers (cm^{-1}) obtained during this study agree with the literature [80, 81]. The band position and the vibrational modes of the samples are summarised in Table 2. All prepared samples showed the characteristic bands of pure hydroxyapatite. Very intense distinctive bands from 952 to 968 cm^{-1} are identified in the Raman spectra of all the synthesised products. These are associated with the symmetrical stretching vibrational (v_1) modes of the tetrahedral phosphate (P–O–P) group. The phosphate ions asymmetric vibrations (v_3) appeared at 1037–1055 cm^{-1}. In addition, the bending vibration (v_2) of PO$_4$ is located around

417–437 cm^{-1}. However, the characteristic bands from 573 to 590 cm^{-1} are allocated to the v_4 bending modes of P–O–P group. Increasing the annealing temperature from 300 °C to 900 °C did not show any change in the hydroxyapatite spectra, thus indicating the synthesis of pure hydroxyapatite (HAP), which did not decompose further into other calcium carbonate components. The -OH group's stretching mode appeared in the 3532–3579 cm^{-1} range. In comparison, the weak broad bands in the HAP might indicate water molecules that may be trapped inside or on the crystallite surface. Regardless of the annealing temperature, all the synthesised samples manifested the appearance of prominent bands of the hydroxyl (OH) and phosphate (PO$_4$$^{3-}$) group. But the Raman spectra of purely biological and natural hydroxyapatite contain a broad band of these vibrational modes along with or without other weak structures. All the samples synthesised by altering the pH confirmed the presence of these characteristic vibrational modes, which attributes to the dominant building units of the biological apatite.
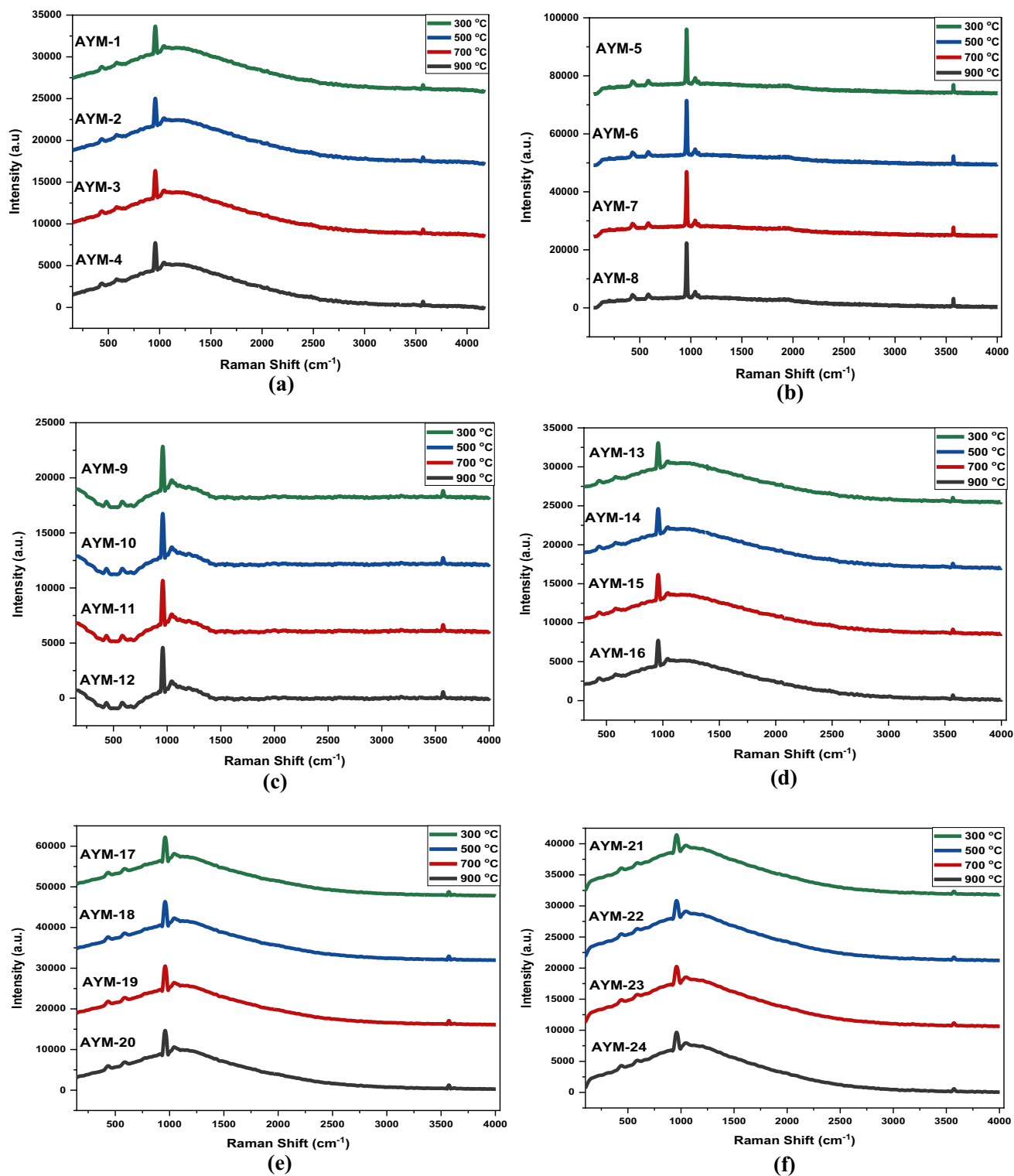
Fig. 4 Raman Spectra of nanohydroxyapatite powders (AYM-1 to AYM-24) prepared at pH **a** 6, **b** 7, **c** 8, **d** 9, **e** 10 and **f** 11 that were calcinated between 300 °C to 900 °C

Table 2 The observed Raman Shift values of the different functional groups present in the prepared hydroxyapatite nanopowders (AYM-1 to AYM-24) obtained at different pH (6–11), and calcination temperature (300 °C–900 °C)

| S. no	pH	Samples codes	Raman shift (cm^{-1}) and type of bonds				OH$^-$	CO$_3^{2-}$
			PO$_4^{3-}$					
			$\sqrt{}_1$ (P-O Symmetric Stretching)	$\sqrt{}_2$ (P-O Stretching)	$\sqrt{}_3$ (P-O asymmetric Stretching)	$\sqrt{}_4$ (P-O Bending)		$\sqrt{}_2$ (C-O) B-type HA
1	6	AYM-1	955	427	1055	579	3573	–
		AYM-2	960	437	1042	581	3574	–
		AYM-3	952	434	1039	581	3569	–
		AYM-4	955	429	1037	584	3566	–
2	7	AYM-5	961	429	1053	581	3545	–
		AYM-6	960	437	1055	571	3542	–
		AYM-7	960	431	1049	576	3532	–
		AYM-8	958	434	1058	573	3539	–
3	8	AYM-9	963	420	1037	590	3574	–
		AYM-10	958	434	1045	585	3569	–
		AYM-11	960	431	1049	582	3567	–
		AYM-12	960	432	1039	589	3562	–
4	9	AYM-13	957	417	1037	574	3571	-
		AYM-14	958	431	1049	581	3569	–
		AYM-15	960	429	1034	579	3563	–
		AYM-16	961	437	1045	573	3558	–
5	10	AYM-17	962	423	1042	581	3569	886
		AYM-18	963	429	1042	579	3565	892
		AYM-19	968	431	1037	590	3571	890
		AYM-20	960	420	1039	593	3574	889
6	11	AYM-21	958	423	1032	579	3579	883
		AYM-22	955	434	1037	581	3568	880
		AYM-23	960	437	1045	590	3564	874
		AYM-24	958	431	1042	584	3565	878

4.4 SEM analysis

The SEM analysis is performed to determine the morphology of the synthesised powders. The observed morphologies achieved by altering the pH are shown in Fig. 5. To obtain different morphologies the acidity and alkalinity of the reaction mixture was fine-tuned. The observed morphology of hydroxyapatite nanopowders in alkaline pH (i.e., 11) is spherical (f). Furthermore, aggregated rods (e), mixed rods/spherical (d), and distorted boxes (c) are observed by changing the pH of the reaction mixture toward low alkalinity (up to 8). However, the hydroxyapatite's nanoflake (b) morphology is observed by decreasing the pH to 7. The beaded rod-like (a) morphology is observed in a weakly acidic medium (pH = 6). Moreover, the particle sizes of the synthesised samples are listed in Table 3. The SEM images have revealed the pH-dependent morphological transition of the prepared samples. From these results, it can be inferred that the pH significantly affects the shape of hydroxyapatite structures.

4.5 EDS analysis

The EDS is used to determine the elemental analysis of the prepared nanohydroxyapatite powders, as depicted in Fig. 6. The EDS is a scientific technique to evaluate the elemental composition of the synthesized material. The spectrogram shows the Kα and Kβ values of the elements present in the prepared structures. This result confirmed that Calcium (Ca), Phosphorus (P), and oxygen are significant elements in the synthesized nanostructures. Therefore, the atomic composition can be estimated by the relative abundance of these three major elements in the prepared samples. From this data, various Ca/P ratios of nanocrystalline hydroxyapatite samples are calculated. Although the observed Ca/P ratios vary from 1.62 to 1.83, these values are relatively close to hydroxyapatite's stoichiometric and theoretical values (1.67) [82].

The fluctuation of values observed for the samples prepared at high pH (10 & 11) is due to the auxiliary (calcium oxide) CaO phase. From this, the EDS analysis confirmed that all the samples are prepared appropriately in the needed Ca/P ratio summarised in Table 4.
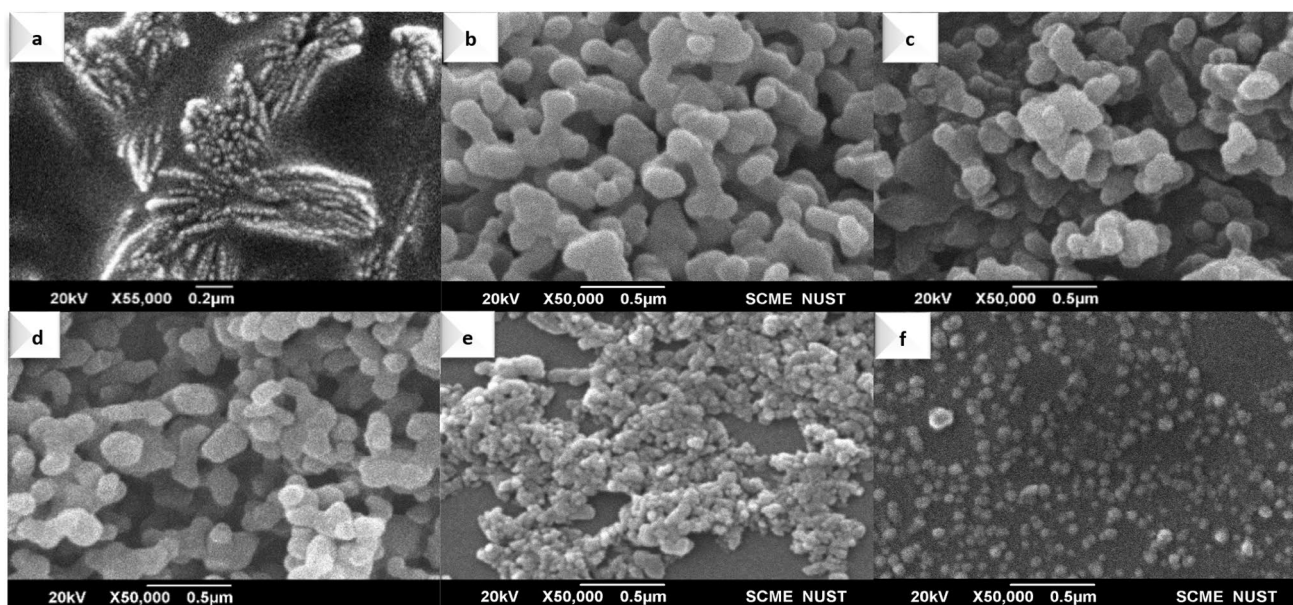
Fig. 5 The Scanning electron microscope (SEM) of the nanometre-sized hydroxyapatite showing the morphologies **a** beaded-rods, **b** nano-flakes, **c** distorted boxes, **d** irregular rods and spherical, **e** aggregated and irregular rods and **f** spherical of powders obtained at different pH annealed at 900 °C

4.6 Effect of pH and annealing temperature on the crystallite size and particle size

To investigate the presence of secondary phase, calcination of the prepared samples (AYM-1 to AYM-24) at different temperatures (300 °C, 500 °C, 700 °C, and 900 °C) is performed. The XRD patterns are compared with the standard hydroxyapatite's diffraction patterns available in the JCPD Standards (JCPDS 74–0566 and 74–0565) as depicted in Fig. 7. The robust and intensive diffraction planes at (002) (211), (112), (300), (211), (213), and (004) verified that all the annealed samples have a hexagonal crystal system close to the pure hydroxyapatite. This confirmed that the calcination temperature did not decompose the composition of the nano-hydroxyapatite structure, and the decreased peak intensities are more pronounced at 300 °C. This fact is illustrated in the XRD diffractogram that the samples prepared at a low temperature of 300 °C have an amorphous phase. The distinction of peaks at low calcination temperatures is more subtle. On the other hand, the poor crystalline phase is observed in the samples annealed at 500 °C. Moreover, the width of the peaks obtained at low calcinating temperatures is comparatively broad; however, increasing the temperature between 700 °C and 900 °C resulted in more distinct and narrower peaks. This distinction of the diffraction peaks exemplified an increased crystallinity fraction at a higher temperature of 900 °C. From these outcomes, it is observed that the elevated temperature enhanced the crystallite size and decreased the width of the peaks, which is a clear indication of improved crystallinity.

Furthermore, the high calcination temperature resulted in the slight shift of the diffraction lines at lower diffraction angles (2Θ) which can be attributed to the increase in the lattice parameters. The crystallite size of all the prepared samples is evaluated using the Debye–Scherrer's mathematical statement, and values are listed in Table 3. The experimentally observed particle and crystallite size of the samples are represented in Fig. 8. From the assessments, we can infer that the size of the sample's particles increased with the annealing temperature.

Recent publications demonstrated that interfacial energy and surface charge are the essential parameters for particle size in solution [83]. These experiments have shown that the ageing of nanoparticles during synthesis by varying the pH systematically affects the particle size. Moreover, the pH is an essential parameter for the dissolution and solubility of different ions in the solution. Furthermore, hydrogen and hydroxyl ions in the solution affect the crystallite and particle size. Due to the protonation and deprotonation of the surface oxygen in the aqueous solution, charged oxides are most likely to be formed. This research group has also explained the formation of small particles at higher pH and ionic strength. Similarly, at pH 11, small spherical particles up to 21.54 nm are observed, as shown in Fig. 5f. In this context, charged surfaces play a dominant role in the stabilisation of the particles. So different researchers have demonstrated semiquantitative models for measuring surface charge as a function of pH to predict particle size variation. The increase in the pH above 9 resulted in the agglomeration of nanoparticles, and it is

Table 3 The observed particle size, crystallite size, and morphology of the hydroxyapatite samples (AYM-1 to AYM-24) prepared at pH (6–11) and annealing temperature (300 °C–900 °C)

S. no.	Reaction pH	Sample (codes)	Crystallite size (nm) $(D)_{hkl}$		Approximate particle size diameter (nm)	Morphology
			Debye–Scherrer	Rietveld refinement		
1	6	AYM-1	10.3	8.74	28.28–42.69	Beaded rod (clusters)
		AYM-2	20.1	18.47		
		AYM-3	44.2	42.52		
		AYM-4	66.9	63.14		
2	7	AYM-5	11.0	9.22	81.10–155.63	Flakes
		AYM-6	23.4	21.65		
		AYM-7	41.3	39.13		
		AYM-8	77.7	75.20		
3	8	AYM-9	9.4	7.54	98.39–202.43	Distorted boxes
		AYM-10	29.9	27.71		
		AYM-11	32.4	30.18		
		AYM-12	71.8	69.30		
4	9	AYM-13	9.1	7.23	86.93–199.84	Irregular rods + spherical
		AYM-14	19.8	17.76		
		AYM-15	39.1	37.67		
		AYM-16	65.2	63.09		
5	10	AYM-17	9.2	8.92	39.32–54.88	Aggregated and irregular rods
		AYM-18	22.3	20.15		
		AYM-19	37.3	35.27		
		AYM-20	61.4	59.45		
6	11	AYM-21	8.4	6.13	21.54–78.89	Spherical
		AYM-22	24.1	21.98		
		AYM-23	31.6	29.05		
		AYM-24	52.8	49.89		

Fig. 6 The EDS of the prepared nanocrystalline hydroxyapatite showing the presence of three important elements, namely: Calcium (Ca), Phosphorus (P), and Oxygen (O)
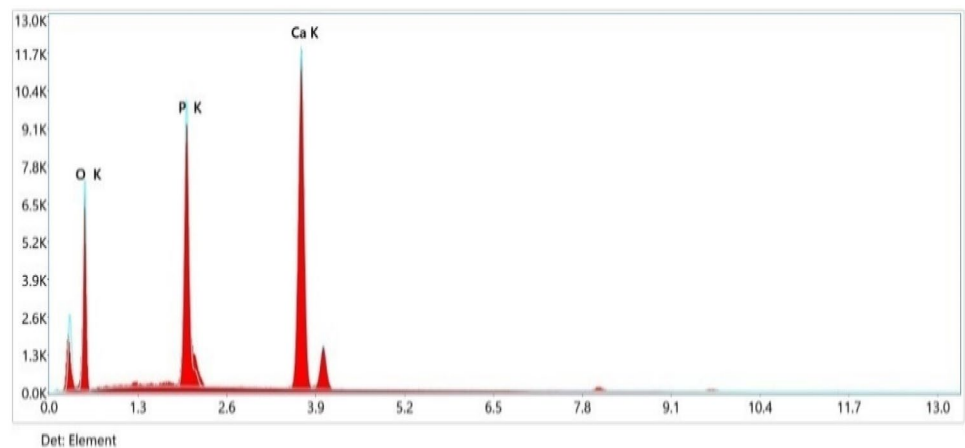
observed during the synthesis of hydroxyapatite up to pH 10, as illustrated in Fig. 5d and e. The small particle sizes up to 28. 28 nm (avg. diameter) of beaded rod HAP is observed at a pH of 6. Still, the lengthwise growth beaded-rods-like clusters are observed in a slightly acidic medium, Fig. 5a.

Furthermore, we found an increase in average particle size up to 202.43 nm (diameter) between pH 7 and 9. With the rise in the pH up to 11, we observed decreased average size of HAP nanopowders. The observed facts suggested a strong correlation between the average particle size and pH.

Table 4 The observed Ca/P ratio derived from EDS analysis of nano-metre-sized hydroxyapatite structures prepared at different pH (6, 7, 8, 9 and 10) calcinated at 900 °C

S. no.	Synthetic condition pH	Elements	Atomic %	Ca/P ratio
1	6	Ca	20.6	1.62
		P	12.7	
2	7	Ca	19.0	1.68
		P	11.3	
3	8	Ca	16.5	1.66
		P	9.9	
4	9	Ca	20.1	1.68
		P	11.9	
5	10	Ca	17.4	1.77
		P	9.8	
6	11	Ca	25.9	1.83
		P	14.1	

5 Discussion

The primary motivation for conducting this study was to understand better the effect of pH on the shape of nanocrystalline hydroxyapatite. The solution's pH is the main parameter to achieve the desired morphology, as the change in the solution's acidity results in the stability of the nanoparticles. The concentration of OH^- and H_3O^+ ions in the solution results in the formation and solubility of the precipitates. During the experiment, the addition of NH_4OH solution into the calcium hydroxide suspension increases the alkalinity of the reaction owing to the release of more hydroxyl (OH^-) ions. Similarly, the seeds (nuclei) act as a framework for crystal growth during the nucleation operation. In this case, these hydroxyl ions are deposited on the facet of developing nuclei in place of Ca^+ and PO_4^{3-} ions produced during the reaction from precursor material [84]. The growth mechanism occurs by changing the solubility of nanoparticles which is size-dependent. Due to the presence of predominant hydroxyl ions at pH 10, agglomerated irregular rods were observed. The tiny nanoparticles have high surface energy and higher solubility rates that redissolve into solution resulting in larger particles that have the potential to grow more [85]—lowering the pH from 10 to 8, decreases the concentration of hydroxyl groups which reduces the saturation of the solution. As a result of it, distorted nanocrystalline structures are formed. Although spherical nanoparticles are observed at pH 11, this particle formation process can be explained on account of the surface energy of the nanoparticles. The energy of the solid's surface depends on the ions (co-ions) present in the solution. So, in the case of oxides, the surface charges are due to the deposition of the

ions. In such a system, hydroxyl ions and protons are the primary charge-determining ions, and the concentration of these ions corresponds to zero, neutral, positive, and negative charge density or vice versa [86, 87]. The surface is negative when the pH is high from the zero-point charge of the oxides resulting in the surface being covered by the OH^- ions, which are the determining ions, and the inverse will be observed in case of more acidic pH. Both opposite charges (determining and counter ions) are present in the solution. Near the surface, the concentration of counter ion is the highest, and far away, it is the lowest, leading to the creation of a double-layered structure [88, 89]. At the same time, the interaction between the particles depends on the surface charge and electric potential at the interface. In the case of spherical nanoparticles, there is no overlap between the double layer, and the electrostatic repulsion is zero between the particles. At lower pH values, alternating the electrical charge at the particle's surface modifies the distribution of both hydroxyl and hydronium ions. While the growth mechanism occurs on the planes where the hydroxyl ions are not present over the surface, therefore at 7 pH, flakes-like morphology is seen. When the concentration of the HPO_4^{2-} increases with the addition of more phosphoric acid (i.e., phosphate-rich media), more binding of HPO_4^{2-} on the facet of developing nuclei results in the formation of negative electric charge, which leads to the decreased crystallite and particle size [51], and beaded rod-like morphology is observed at pH 6. Many stoichiometric phases of hydroxyapatite (calcium phosphate) were synthesized by this protocol with varying Ca/P ratios between 1.62 and 1.83. We believe that the samples synthesised at pH 7, 8, and 9 has a Ca/P ratio of 1.66 -1.68, almost similar to the theoretical value of bone apatite (1.677). These Ca/P ratios at pH (6, 7, 8, 9, 10, and 11) annealed at 900 °C also agree with the values provided in the literature [90]. Hydroxyapatite with different Ca/P molar ratio has an effect on the properties of the biomaterial and exhibits structural, optical and dielectric characteristics [91, 92]. The deviation in the Ca/P ratio from the stoichiometric ratio of bone apatite is mainly ascribed to the presence of other interfering ions. In addition to this, increasing the calcination temperature from 300 °C of the samples (AYM-4, AYM-8, AYM-12, AYM-16, AYM-20, and AYM-24) to 900 °C influenced the formation of large crystallites up to 77.7 nm, this phenomenon can be explained on account of enhanced rate of deposition reaction and resulting crystallites sinter together that culminated in the formation of large-sized crystallites [93]. The nucleation rate is affected by the solubility limit of the charged species during co-precipitation. As a result, the degree of supersaturation favours the formation of large and small crystals in the solution. The more supersaturation, the smaller will be the crystal size. Inverse
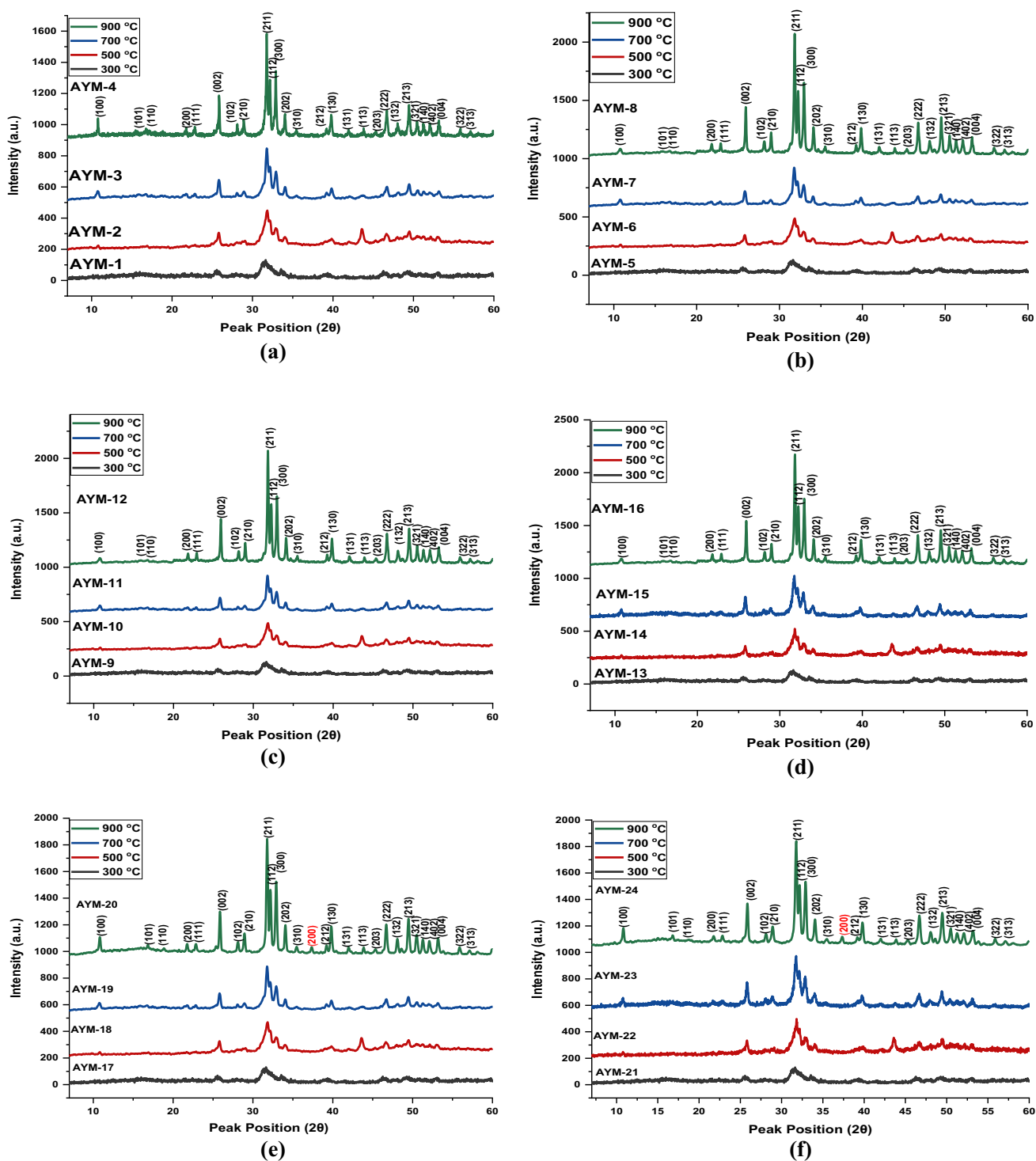
Fig. 7 XRD diffractogram of hydroxyapatite nano-powders (AYM-1 to AYM-24) obtained at various annealing temperatures (300 °C, 500 °C, 700 °C and 900 °C) and pH **a** 6, **b** 7, **c** 8, **d** 9, **e** 10, and **f** 11 (Reference pattern: JCPDS 74-0566, JCPDS 74-0565)

phenomena can be observed in the slightly acidic medium [94]. The same trend is observed at a higher pH, and the crystallite size is between 8.4 and 52.8 nm. A slightly large crystallite size between 11.0 and 77.7 nm is attained at neutral pH. However, the colloidal particles resisted coarsening when the interfacial energy approached zero. As a result, no increase in the particle size is observed after pH
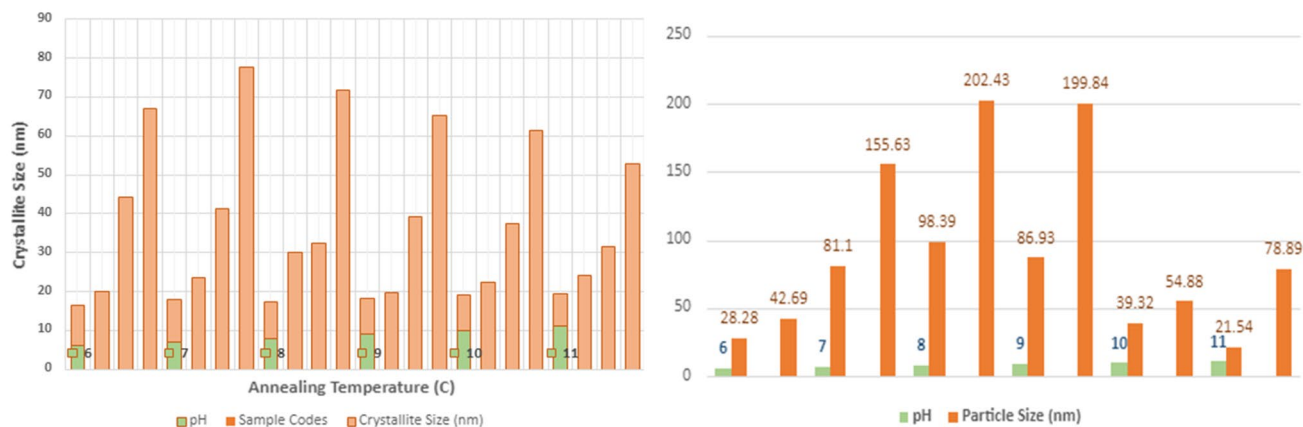
Fig. 8 (Left side) The observed crystallite size (nm) by changing the annealing temperature between 300 °C and 900 °C at pH 6–11, and (right side) the observed particle sizes (nm) of synthesised samples calcinated at 900 °C concerning the pH. Both graphical representations are for the samples prepared at pH 6, 7, 8, 9, 10, and 11 (indicated by green colour)

7 (i.e., at pH = 8, 9 & 10), indicating that Ostwald ripening did not occur at higher pH.

Furthermore, it is worth mentioning that the shape and size of the nanoparticles have significant clinical applications, such as in phototherapy for cancer treatment [52]. Previous research on bone tissue regeneration revealed that HAP morphology influences bone cells' viability and activity. In this regard, an in-vitro study demonstrated that the nanorod-like morphology of hydroxyapatite induced apoptosis in malignant VX2 cancer cells. They illustrated the results of the enhanced attachment and proliferation of the human osteoblast cells (HOB) over rod-like hydroxyapatite nanoparticles (50–80 nm long). In addition, the high contact of HA nanoparticles with the macrophages led to the minimal release of lactate dehydrogenase (LDH) and inflammatory cytokine (TNF- α) [95]. In contrast, the needled-shaped morphology of hydroxyapatite induced the most significant inhibition and apoptosis due to the mechanical stresses on the cell surface. Moreover, it is reported that the long rod-shaped HAP has a decreased apoptosis rate than the short rod-shaped HAP [67]. Similarly, the spherical-shaped hydroxyapatite nanoparticles were found to have a reduced rate of osteoblast cell proliferation compared with long rod-shaped HAP nanoparticles [96]. In this context, smooth spherical granules [97], rod-like [98], ellipsoidal [99] and plate-like [100] morphology of hydroxyapatite have a significant role in the growth and proliferation of osteoblast cells. It is noteworthy that hydroxyapatite's morphology is essential in drug delivery. In addition, a group of researchers illustrated the effect of smooth spherical granules for faster bone growth and demonstrated the enhanced drug release rate by generating less inflammatory response than irregularly shaped hydroxyapatite granules [101]. The mesoporous rod-like [102, 103], needle or plate-shaped [104], porous spherical [105] and nanorod-assembled hollow polyhedral

[106] hydroxyapatite have been reported as a suitable candidate for the osteogenic growth, antibiotic, and anticancer drug delivery due to their high loading capacity and sustained release.

Furthermore, the nanometric crystalline structures influence cellular interaction and have remarkable biomedical applications [107]. Additionally, these specific characteristics have introduced the possibility of modulating the applications of hydroxyapatite other than biomedical such as materials for environmental remediation, packing material in column chromatography, gas sensing, and in different electrical and optical industries [108].

6 Conclusion

Morphologically and structurally different hydroxyapatite nanopowders are successfully prepared by the wet-chemical precipitation method. Therefore, the reported methodology is appropriate for preparing morphologically distinct hydroxyapatites. However, the effect of pH and annealing temperature was investigated through SEM, XRD, FTIR, and Raman spectroscopy. From these investigations, it can be concluded that the high-purity and single crystalline phase of nano-hydroxyapatite powders were synthesised below pH 10. However, increasing the alkalinity between pH 6 and 10 enhanced the particle size from 21.54 to 202.43 nm. Furthermore, all peaks in the XRD diffractograms can be perfectly indexed to the stable hexagonal phase of hydroxyapatite below pH 10. Similarly, the secondary CaO phase and enhanced Ca/P ratio were observed at a more alkaline medium (10 and 11). Different morphologies, from beaded rods to spherical nanoparticles, were observed by altering the pH from weakly acidic to a basic medium.

Moreover, the average crystallite size increases from 8.4 nm to 77.7 nm upon heat treatment. Therefore, it is concluded that the solution's acidity and alkalinity (pH) have a more pronounced influence on the particle size and morphology than the crystallite size. In contrast to this, calcination has a substantial impact on crystallite size.

Author contributions Postulation and approach, ZH and UL; design, investigation and data formulation, AAA; prototypical draft-editing, AAA; supervision, visualization and project administration, UL and ZH. All authors have scrutinized and agreed to the edited description of the manuscript.

Declarations

Conflict of interest The authors declare no known external competing financial interests or personal correspondence that could have appeared to dominate the work proclaimed in this paper.

References

1. D.K. Dubey, V. Tomar, Mater. Sci. Eng. C **29**, 7 (2009). https://doi.org/10.1016/j.msec.2009.04.015
2. C. Szpalski, M. McRae, G.F. Rogers, J.D. Bumgardner, S.M. Warren, Compreh. Biomater. (2011). https://doi.org/10.1016/B978-0-08-055294-1.00219-1
3. K.R. Paweł, J. Hadzik, J. Seeliger, K. Kozak, K. Jurczyszyn, H. Gerber, M. Dominiak, C. Kunert-Keil, Ann. Anat. Anato. Anz. (2017). https://doi.org/10.1016/j.aanat.2017.05.010
4. R.V. Silva, J.A. Camilli, C.A. Bertran, N.H. Moreira, Int. J. Ora Maxillo Surg. **34**, 2 (2005). https://doi.org/10.1016/j.ijom.2004.06.005
5. S. Mondal, S.V. Dorozhkin, U. Pal, Nanomed. Nanobiotech. **10**, 4 (2017). https://doi.org/10.1002/wnan.1504
6. G. Bharath, S.L. Beeseti, N. Ponpandian, A. Faheem, S. Muheet, H. Abdel, A. Saleh, M. Lamjed, A. Edreese, Nanomaterials **7**, 6 (2017). https://doi.org/10.3390/nano7060138
7. B. Palazzo, M. Iafisco, M. Laforgia, N. Margiotta, G. Natile, C.L. Bianchi, D. Walsh, S. Mann, N. Roveri, Adv. Func. Mater. **17**, 13 (2007). https://doi.org/10.1002/adfm.200600361
8. G.L. de Lange, K. Donath, Biomaterials **10**, 2 (1989). https://doi.org/10.1016/0142-9612(89)90044-6
9. C. Auclair-Daigle, M.N. Bureau, J.G. Legoux, L.H. Yahia, J. Biomed. Mater. Res. A **73**, 4 (2005). https://doi.org/10.1002/jbm.a.30284
10. W. S. W. Harun, R. I. M. Asri, A. B. Sulong, S. A. C. Ghani, Z. Ghazalli, in Advances in Composite Biomaterials ed By J. Thirumalai (Biomedical Application -Technology Facet, Intechopen, 2018). http://doi.org/https://doi.org/10.5772/intechopen.71063.
11. K. Søballe, Acta Orthop. Scand. Suppl. **64**, 255 (1993). https://doi.org/10.3109/17453679309155636
12. M. S. Islam, M. A. A. Mamun, A. Khan, M. Todo, ed by P. Vizureanu, C. M. D. C. F. Botelho, (Intechopen, Biomaterial, 2020). https://doi.org/10.5772/intechopen.92900.
13. S. Teixeira, M.A. Rodriguez, P. Pena, A.H. De Aza, S. De Aza, M.P. Ferraz, F.J. Monteiro, Mater. Sci. Eng. C **29**, 5 (2009). https://doi.org/10.1016/j.msec.2008.09.052
14. H. Ghomi, M.H. Fathi, H. Edris, J. Sol-Gel Sci. Technol. **58**, 3 (2011). https://doi.org/10.1007/s10971-011-2439-2
15. S. Mondal, U. Pal, J. Drug Delivery Sci. Technol. **53**, 101131 (2019). https://doi.org/10.1016/j.jddst.2019.101131
16. S.C. Cox, J.A. Thornby, G.J. Gibbons, M.A. Williams, K.K. Mallick, Mater. Sci. Eng. C Mater. Bio. App. **47**, 237 (2015). https://doi.org/10.1016/j.msec.2014.11.024
17. R.I. Martin, P.W. Brown, Mechanical properties of hydroxyapatite formed at physiological temperature. J. Mater. Sci. Mater. Med. **6**, 3 (1995). https://doi.org/10.1007/bf00120289
18. A.E. Hannora, S. Ataya, J. Alloys Compd. (2016). https://doi.org/10.1016/j.jallcom.2015.10.240
19. S. Pramanik, A.K. Agarwal, K.N. Rai, A.J. Garg, Ceram. Int. **33**, 3 (2007). https://doi.org/10.1016/j.ceramint.2005.10.025
20. M. Chang, B.G. Kim, J.H.J. Whang, Korean Ceram. Soc. (2020). https://doi.org/10.1007/s43207-020-00026-z
21. C.A. van Blitterswijk, S.C. Hesseling, J.J. Grote, H.K. Koerten, K. de Groot, J. Biomed. Mater. Res. **24**, 4 (1990). https://doi.org/10.1002/jbm.820240403
22. H. Wang, Y. Li, Y. Zuo, J. Li, S. Ma, L.J. Cheng, Biomaterials **22**, 28 (2007). https://doi.org/10.1016/j.biomaterials.2007.04.014
23. R. Ma, D. Guo, J. Orthop. Surg. Res. **32**, 14–21 (2019). https://doi.org/10.1186/s13018-019-1069-1
24. H.J. Reza, S.R. Mohsen, A.M. Eiman, E. Marzieh, Arab. J. Sci. Eng. (2017). https://doi.org/10.1007/s13369-017-2498-y
25. H. Zhang, Y. Yan, Y. Wang, S. Li, Adv. Eng. Mater. **4**, 12 (2002). https://doi.org/10.1002/adem.200290003
26. M.R. da Cunha, V.O. Gushiken, J.P.M. Issa, A. Iatecola, M. Pettian, A.R. Santos, J. Craniofac. Surg. **22**, 6 (2011). https://doi.org/10.1097/scs.0b013e3182319876
27. S.H. Kim, C.H. Park, J.H. Heo, J.H. Lee, J. Korean Ceram. Soc. (2022). https://doi.org/10.1007/s43207-022-00198-w
28. C. Liu, W. Wang, W. Shen, T. Chen, L. Hu, Z. Chen, J. Endod. **23**, 8 (1997). https://doi.org/10.1016/s0099-2399(97)80307-x
29. R.Z. Legeros, in Bioceramics and their Clinical Applications, ed By T. Kokubo (Clinical Application of Bioceramic, ScienceDirect, 2008). https://doi.org/10.1533/9781845694227.2.367
30. N.M. Pu'ad, P. Koshy, H.Z. Abdullah, M.I. Idris, T.C. Lee, Heliyon **5**, 5 (2019). https://doi.org/10.1016/j.heliyon.2019.e01588
31. G. Ma, IOP Conf. Ser. Mater. Sci. Eng. **668**, 3 (2019). https://doi.org/10.1088/1757-899X/688/3/033057
32. R.R. Rao, H.N. Roopa, T.S. Kannian, J. Mater. Sci. Mater. Med. **8**, 8 (1997). https://doi.org/10.1023/a:1018586412270
33. R.K. Shah, M.N. Fahmi, A.H. Mat, A.A. Zainal, Med. J. Malaysia **59**(Suppl B), 75–76 (2004). (**PMID: 15468826**)
34. S.S.A. Abidi, Q. Murtaza, J. Mat. Sci. Tech. **30**, 4 (2014). https://doi.org/10.1016/j.jmst.2013.10.011
35. S.C. Wu, H.C. Hsu, M.Y. Liu et al., J. Korean Ceram. Soc. (2021). https://doi.org/10.1007/s43207-020-00087-0
36. F. Cestari, F. Agostinacchio, A. Galotta, G. Chemello, A. Motta, V.M. Sglavo, Nanomaterials **11**, 2 (2021). https://doi.org/10.3390/nano11020264
37. G. Bezzi, G. Celotti, E. Landi, T.M.G. La Torretta, I. Sopyan, A. Tampieri, Mater. Chem. Phys. **78**, 3 (2003). https://doi.org/10.1016/s0254-0584(02)0039
38. H.S. Liu, T.S. Chin, L.S. Lai, S.Y. Chiu, K.H. Chung, C.S. Chang, M.T. Lui, Ceram. Int. **23**, 1 (1997). https://doi.org/10.1016/0272-8842(95)00135-2
39. J.S. Cho, Y.C. Kang, J. Alloys Compd. **464**, 1–2 (2008). https://doi.org/10.1016/j.jallcom.2007.09.092
40. M. Canillas, R. Rivero, R.G. Carrodeguas, B. Flora, M.A. Rodríguez, Boletín de la Sociedad Española de Cerámica y Vidrio **56**, 5 (2017). https://doi.org/10.1016/j.bsecv.2017.05.002
41. C. Durucan, P.W. Brown, J. Mater, Sci. Mater. Med. **11**, 6 (2000). https://doi.org/10.1023/a:1008934024440

42. W. Kim, F. Saito, Ultrason. Sonochem. **8**, 2 (2001). https://doi.org/10.1016/s1350-4177(00)00034-1

43. E.J.P. Gérrard, K.G. Malay, N. Yan-Jing, B.I. Touma, S. Anand, P. Singh, J. Hazard. Mater. **185**, 1 (2011). https://doi.org/10.1016/j.jhazmat.2010.08.087

44. J. Liu, X. Ye, H. Wang, M. Zhu, B. Wang, H. Yan, Ceram. Int. **29**, 6 (2003). https://doi.org/10.1016/s0272-8842(02)00210-9

45. R. Zhu, R. Yu, J. Yao, D. Wang, J. Ke, J. Alloys Comp. **457**, 1–2 (2008). https://doi.org/10.1016/j.jallcom.2007.03.081

46. P. Szterner, M. Biernat, J. Therm. Anal. Calorim. (2022). https://doi.org/10.1007/s10973-022-11564-5

47. P. Szterner, B. Biernat, Bioinorg. Chem. App. (2020). https://doi.org/10.1155/2022/3481677

48. I.H. Lee, J.A. Lee, J.H. Lee, Y.W. Hoe, J.J. Kim, J. Korean Ceram. (2020). https://doi.org/10.1007/s43207-019-00004-0

49. A. Yudin, I. Ilinykh, K. Chuprunov, E. Kolesnikov, D. Kuznetsov, D. Leybo, A. Godymchuk, J. Phys. Conf. Ser. **1145**, 1 (2019). https://doi.org/10.1088/1742-6596/1145/1/012003

50. K. Chuprunov, A. Yudin, D. Lysov, E. Kolesnikov, D. Kuznetsov, D. Leybo, I. Ilinykh, A. Godymchuk, IOP Conf. Ser. Matter. Sci. Eng. (2020). https://doi.org/10.1088/1757-899X/731/1/012023

51. S.L. Ortiz, D.M. Anaya, D.S. Campos, M.E.F. GarcÃa, E.S. RodrÃ-guez, M.I.R. Valderrama, V. RodrÃguez-Lugo, R. Arenal, J. Nanomater. **2020**, 1–10 (2020). https://doi.org/10.1155/2020/5912592

52. B. Ankamwar, in Biomedical Engineering ed By R.Hudak, M. Penhaker, J. Majernik (Biotechnology, Intechopen, 2012).

53. S. Dey, M. Das, V.K. Balla, Mater. Sci. Eng. C Mater. Biol. Appl. **39**, 1 (2014). https://doi.org/10.1016/j.msec.2014.03.022

54. X. Gui, W. Peng, X. Xu, Z. Su, G. Liu, Z. Zhou, M. Liu, Z. Li, G. Song, C. Zhou, O. Kong, Nanotech. Rev. **11**, 1 (2022). https://doi.org/10.1515/ntrev-2022-0127

55. S.H. Chu, D.F. Feng, Y.B. Ma, Z.Q. Li, Int. J. Nanomed. (2012). https://doi.org/10.2147/IJN.S33584

56. C. Kim, J.W. Lee, J.H. Heo, C. Park, D.H. Kim, G.S. Yi, H.C. Kang, H.S. Jung, H. Shin, J.H. Lee, Biomater. Res. **26**, 7 (2022). https://doi.org/10.1186/s40824-022-00253-x

57. N.I. Farkas, G.L. Turdean, L. Bizo, L. Marincaș, O. Cadar, L. Barbu-Tudoran, B. Réka, Ceram. Int. (2023). https://doi.org/10.1016/j.ceramint.2023.05.047

58. L.F. Sukhodub, L.B. Sukhodub, A.D. Pogrebnjak, T. Amanzhol, A. Kistaubayeva, I. Savitskaya, D.J. Shokatayeva, Korean Ceram. Soc. **57**, 557–569 (2020). https://doi.org/10.1007/s43207-020-00061-w

59. Z. Shi, X. Huang, Y. Cai, R. Tang, D. Yang, Acta Biometer. **5**, 1 (2009). https://doi.org/10.1016/j.actbio.2008.07.023

60. S. Dey, M. Das, V.K. Balla, Mater. Sci. Eng. C (2014). https://doi.org/10.1016/j.msec.2014.03.022

61. X. Chen, C. Deng, S. Tang, M. Zhang, Biol. Pharm. Bull. **30**, 1 (2007). https://doi.org/10.1248/bpb.30.128

62. J. Jin, G. Zuo, G. Xiong, H. Luo, Q. Li, C. Ma, D. Li, F. Gu, Y. Ma, Y. Wan, J. Mater. Sci. **25**, 4 (2014). https://doi.org/10.1007/s10853-013-5126-8

63. S. Ezhaveni, R. Yuvakkumar, M. Rajkumar, N.M. Sundaram, V. Rajendran, J. Nanosci. Nantechnol. **13**, 3 (2013). https://doi.org/10.1166/jnn.2013.7135

64. H. Gao, W. Shi, L.B. Freund, Proc. Natl. Acad. Sci. **102**, 27 (2005). https://doi.org/10.1073/pnas.0503879102

65. S.Y. Lee, M. Ferrari, P. Decuzzi, Nanotechnology **29**, 49 (2009). https://doi.org/10.1088/0957-4484/20/49/495101

66. G. Adriani, M.D. de Tullio, M. Ferrari, F. Hussain, G. Pascazio, X. Liu, P. Decuzzi, P. Biomater. (2012). https://doi.org/10.1016/j.biomaterials.2012.04.027

67. Z. Xu, C. Liu, J. Wei, J. Sun, J. Appl. Toxicol. **32**, 6 (2012). https://doi.org/10.1002/jat.1745

68. M.H. Hong, J.S. Son, K.M. Kim, M. Han, D.S. Oh, Y.K. Lee, J. Mater. Sci. Mater. Med. **22**, 2 (2011). https://doi.org/10.1007/s10856-010-4197-z

69. W. Zhang, Y. Chai, X. Xu, Y. Wang, N. Cao, Appl. Surf Sci. **322**, 71–77 (2014)

70. G.D. Venkatasubbu, S. Ramasamy, V. Ramakrishnan, J. Kumar, J. Biomed. Nanotechnol. **7**, 6 (2011). https://doi.org/10.1166/jbn.2011.1350

71. G.S. Albahy, Y.M. Abbas, A.M. Hezma, N. Gweily, J. Text Color Polym. **17**, 2 (2020). https://doi.org/10.21608/JTCPS.2020.32002.1041

72. M.H. Santos, M. de Oliveira, L.P. de Freitas, H.S. Mansur, W.L. Vasconcelos, Mater. Res. **7**, 4 (2004). https://doi.org/10.1590/S1516-14392004000400017

73. M. Tahriri, M. Solati-Hashjin, H. Eslami, Iran. J. Pharm. Sci. **4**, 2 (2008). (**ISSN: 1735-2444**)

74. H.R. Javadinejad, R.M. Saboktakin, M.E. Aghababaei, Arab. J. Sci. Eng. (2017). https://doi.org/10.1007/s13369-017-2498-y

75. S.M. Rizi, H. Minouei, B.J. Lee, H. Pouraliakbar, M.R. Toroghinejad, S.I. Hong, Mater. Sci. Eng. A (2021). https://doi.org/10.1016/j.msea.2021.141803

76. R.M. Saboktakin, H. Minouei, B.J. Lee, M.R. Toroghinejad, S.I. Hong, J. Alloy Comp. (2022). https://doi.org/10.1016/j.jallcom.2022.165108

77. M. Ahmadipour, K. Rao, K.V. Rajendar, J. Nanomater. (2012). https://doi.org/10.1155/2012/163909

78. S. Gao, K. Sun, A. Li, H. Wang, Mater. Res. Bull. **48**, 3 (2013). https://doi.org/10.1016/j.materresbull.2012.11.090

79. H.W. Fern, M.N. Salimi, AIP Conf. Proc. Green Design Manuf. **2339**, 1 (2021). https://doi.org/10.1063/5.0044252

80. J.K. Abifarin, D.O. Obada, E.T. Dauda, D. Dodoo-Arhin, Data Br. (2019). https://doi.org/10.1016/j.dib.2019.104485

81. V.V. Nosenko, A.M. Yaremko, V.M. Dzhagan, I.P. Vorona, Y.A. Romanyuk, I.V. Zatovsky, J. Raman Spec. **47**, 6 (2016). https://doi.org/10.1002/jrs.4883

82. U. Tariq, Z. Haider, K. Chaudhary, R. Hussain, J. Ali, J. Phys. Conf. Ser. **1027**, 1 (2018). https://doi.org/10.1088/1742-6596/1027/1/012015

83. G. Arandhara, J. Bora, P.K. Saikia, Mater. Chem. Phys. (2020). https://doi.org/10.1016/j.matchemphys.2019.122277

84. V.R. Lugo, T.V.K. Karthik, D. Mendoza-Anaya, E. Rubio-Rosas, L.S. Villaseñor Cerón, M.I. Reyes-Valderrama, E. Salinas-Rodríguez, R. Soc. Open Sci. (2018). https://doi.org/10.1098/rsos.180962

85. N.T.K. Thanh, N. Maclean, S. Mahiddine, Chem. Rev. **114**, 15 (2014). https://doi.org/10.1021/cr400544s

86. H. Van Olphen, Zeta potential in colloid science—theory and application, in *Clays and clay minerals*. ed. by R.J. Hunter (Academic Press, London, 1982), p.159

87. V. Selvamani, Stability studies on nanomaterials used in drugs, in *Characterization and biology of nanomaterials for drug delivery*. ed. by S.S. Mohapatra, S. Ranjan, N. Dasgupta, R.K. Mishra, S. Thomas (Elsevier, Amsterdam, 2019), pp.425–444

88. K.S. Birdi, *Controlled Synthesis and Processing of Ceramic Oxides—A Molecular Approach*, 3rd edn. (Handbook of Surface and Colloid Chemistry, CRC Press, Boca Raton, 2008). https://doi.org/10.1201/9781420007206

89. I.S. Sidhu, A.L. Frischknecht, P.J. Atzberger, ACS Omeg. **3**, 9 (2018). https://doi.org/10.1021/acsomega.8b01393

90. C. Rey, Comp. Biomater. II (2017). https://doi.org/10.1016/b978-0-12-803581-8.10171-7

91. S.J. Kashyap, R. Sankannavar, G.M. Madhu, J. Korean Ceram. Soc. (2022). https://doi.org/10.1007/s43207-022-00225-w

92. S. Ramesh, C.Y. Tan, M. Hamdi, I. Sopyan, W.D. Teng, S. Du, J. Leng, A.K. Asundi, SIPE Inter. Conf. Smart Mater. Technol. (2007). https://doi.org/10.1117/12.779890

93. K.E. Öksüz, S. Kilinç, A. Özer, Trans. Ind. Ceram. Soc. **78**, 1 (2019). https://doi.org/10.1080/0371750X.2019.1588170

94. M. Tsega, F.B. Dejene, Helivon (2017). https://doi.org/10.1016/j.heliyon.2017.e00246

95. K. Zhang, Y. Zhou, C. Xiao, W. Zhao, H. Wu, J. Tang, Z. Li, S. Yu, X. Li, L. Min, Z. Yu, G. Wang, L.L. Wang, K. Zhang, X. Yang, X. Zhu, C. Tu, X. Zhang, Sci. Adv. **5**, 8 (2019). https://doi.org/10.1126/sciadv.aax6946

96. N.K. Nga, L.T. Giang, T.Q. Huy, P.H. Viet, C. Migliaresi, Colloids Surf. B (2014). https://doi.org/10.1016/j.colsurfb.2013.11.001

97. H.H. Lee, S.J. Hong, C.H. Kim, E.C. Kim, J.H. Jhang, H.I. Shin, H.W. Kim, J. Mater. Sci. Mater. Med. (2008). https://doi.org/10.1007/s10856-008-3435-0

98. G. Montalbano, G. Molino, S. Fiorilli, C. Vitale-Brovarone, J. Eur. Ceram. **40**, 11 (2020). https://doi.org/10.1016/j.jeurceramsoc.2020.02.018

99. M.Y. Ma, Y.J. Zhu, L. Li, S.W. Cao, J. Mater. Chem. (2008). https://doi.org/10.1039/B800389K

100. B. Viswanath, N. Ravishankar, Biomaterials **29**, 36 (2008). https://doi.org/10.1016/j.biomaterials.2008.09.001

101. W. Paul, C.P. Sharma, J. Mater. Sci. Mater. Med. (1999). https://doi.org/10.1023/a:1008918412198

102. S. Liu, J. Wang, J. Chen, S. Guan, T. Zhang, Biomater. Adv. (2022). https://doi.org/10.1016/j.bioadv.2022.212821

103. S. Safi, F. Karimzadeh, S. Labbaf, Mater. Sci. Eng. C (2018). https://doi.org/10.1016/j.msec.2018.07.004

104. B. Palazzo, M. Iafisco, M. Laforgia, N. Margiotta, G. Natile, C.L. Bianchi, D. Walsh, S. Mann, N. Roveri, Adv. Funct. Mater. **17**, 13 (2007). https://doi.org/10.1002/adfm.200600361

105. V.S. Komlev, S.M. Barinov, E.V. Koplik, Biomaterials **23**, 16 (2002). https://doi.org/10.1016/S0142-9612(02)00049-2

106. Y.D. Yu, Y.J. Zhu, C. Qi, Y.Y. Jiang, H. Li, J. Wu, J. Colloid Interface Sci. (2017). https://doi.org/10.1016/j.jcis.2017.02.041

107. S. Lara-Ochoa, W. Ortega-Lara, C.E. Guerrero-Beltrán, Physicochem. App. Pharm. **1642**, 13 (2021). https://doi.org/10.3390/pharmaceutics13101642

108. M. Ibrahim, M. Labaki, J.M. Giraudon, J.F. Lamonier, J. Hazard. Mater. (2020). https://doi.org/10.1016/j.jhazmat.2019.121139